

Space CoBot: modular design of an holonomic aerial robot for indoor microgravity environments

Pedro Roque¹ and Rodrigo Ventura¹

Abstract—This paper presents the design of a small aerial robot for inhabited microgravity environments, such as orbiting space stations (e.g., ISS). In particular, we target a fleet of robots, called Space CoBots, for collaborative tasks with humans, such as telepresence and cooperative mobile manipulation. The design is modular, comprising an hexarotor based propulsion system, and a stack of modules including batteries, cameras for navigation, a screen for telepresence, a robotic arm, space for extension modules, and a pair of docking ports. These ports can be used for docking and for mechanically attaching two Space CoBots together. The kinematics is holonomic, and thus the translational and the rotational components can be fully decoupled. We employ a multi-criteria optimization approach to determine the best geometric configuration for maximum thrust and torque across all directions. We also tackle the problem of motion control: we use separate converging controllers for position and attitude control. Finally, we present simulation results using a realistic physics simulator. These experiments include a sensitivity evaluation to sensor noise and to unmodeled dynamics, namely a load transportation.

I. INTRODUCTION

Multirotor vehicles have recently gained widespread use in various application areas, such as transportation, surveillance, and even entertainment. These platforms are mechanically simple and typically lightweight, resulting in a low cost of acquisition and maintenance. However, to the best knowledge of the authors, there is no known application of multirotor vehicles in space environments. Discarding the obvious impossibility of maneuvering in the absence of air, we consider here the use of these vehicles in human-compatible pressurised spaces under microgravity, such as inside inhabited space stations.

The idea of aerial vehicles inside space stations is not new. The NASA project SPHERES (Synchronized Position Hold Engage Reorient Experimental Satellites) started in 2000 with the design of a small pressurised air propulsion vehicle [1]. In 2006 three SPHERES units were deployed aboard the International Space Station (ISS) [2]. However, the use of pressurised air makes the mechanical complexity significantly higher than a multirotor based solution. More recently, NASA proposed the Astrobee vehicle, with a simpler propulsion system based on several centrifugal fans and nozzles [3]. The Astrobee also features a 2 DoF arm and

docking capability. However, most of its volume (about 67%) and area (about 56%) are occupied by the propulsion system, where each fan requires an unobstructed duct from side to side.

The most prominent feature of these spaces is the negligible effect of gravity, called microgravity, resulting from the orbital motion of the space station around the planet. We will exploit this feature in the following way. Most multirotor orient their propellers vertically along parallel axes. This maximizes thrust vertically in order to compensate for the gravity force. However, in doing so they need to tilt in order to move sideways. Moreover, most of the energy is spent in compensating for gravity. In its absence, not only there is no need to compensate for gravity, but also the energy consumption is expected to be significantly less. We propose to orient the propeller rotation axes non-parallel among them, in such a way we obtain a fully holonomic vehicle. We expect to increase maneuverability, being a particularly relevant feature inside confined spaces such as the interior of a space station.

Holonomic multirotors have been proposed in the past, but the literature is scarce. In [4], [5] a dexterous hexarotor has been proposed, where the holonomic kinematics is used for dexterous manipulation. However, this vehicle is designed for Earth applications, and thus a trade-off is necessary between dexterity and gravity compensation. Our design is also based in an hexarotor, but since we consider microgravity, we will design the propeller orientation in order to maximize maneuverability along all directions. Related work in design optimization of hexrotors can be found in [6], [7] while in [8] a variable pitch solution is proposed.

The goal of this paper is to present a design of a aerial robot for microgravity environments. We target a modular and multipurpose vehicle, providing, for instance, (1) telepresence, requiring the vehicle to manoeuvre in such a way the screen and camera is pointed towards the party onboard, and (2) mobile manipulation, requiring force closure in order to compensate the reaction force at the end effector. Our design also includes a docking port for docking into a charging station and stacking of multiple units for, e.g., combined thrust.

This paper is structured as follows: the proposed design is detailed in Section II, in Section III we derive a parametric model of the propulsion system, which is then used in Section IV for the optimization its parameters. Section V presents a dynamical model of the vehicle together with a convergent controller for this holonomic vehicle, and a preliminary validation in a realistic simulation environment

*The authors are grateful to André Santos for the CAD modeling of the vehicle and the renderings presented in this paper. This work was supported by the FCT project [UID/EEA/50009/2013].

¹Pedro Roque and Rodrigo Ventura are with Institute for Systems and Robotics, Instituto Superior Técnico, Universidade de Lisboa, Av. Rovisco Pais, 1, 1049-001 Lisboa, Portugal. pedro.roque@tecnico.ulisboa.pt, rodrigo.ventura@isr.tecnico.ulisboa.pt

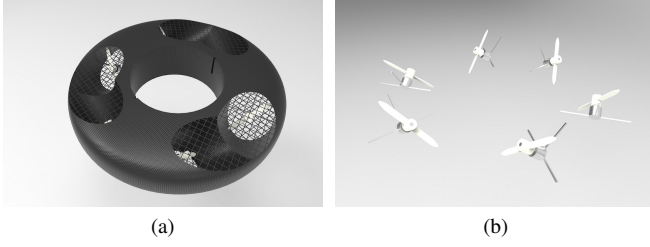


Fig. 1: Propulsion system representation: (a) overall view of the module, and (b) relative placement of the propellers.

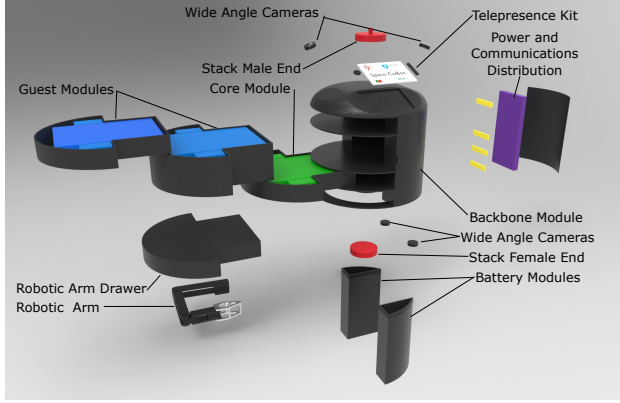


Fig. 2: Overall view of Space Cobot modules.

is presented in Section VI, while Section VII wraps up the paper with concluding remarks and a reference for future work.

This paper builds upon and extends an early draft available in arXiv [9].

II. VEHICLE DESIGN

As space operation is expensive, we target a modular vehicle whose parts can be easily maintained and that is easily extensible with additional modules, e.g., hosting of scientific experiment testbeds. An overview of all the modules is provided in Figure 2 and explained below.

To provide propulsion to the vehicle, we use 6 electric motors with 4" propellers, arranged in such a way the kinematics is holonomic. We defer a detailed description of this system, along with its optimization, to Sections III and IV. Our design of this system is shown in Figure 1.

The propulsion module attaches to the central core of the vehicle, a backbone module, that provides support for all remaining subsystems: batteries, a pair of docking connectors, cameras, extension modules, telepresence equipment, and a robotic manipulator.

For positioning inside the station we propose a vision-based localization method employing 4 wide-angle cameras, two on the top side of the vehicle and two on the bottom. These cameras also enable visual servoing of the robotic arm. Autonomous navigation is delivered by onboard computation, the Core module, capable of video processing

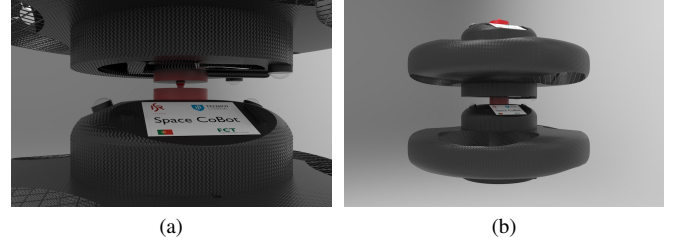


Fig. 3: Space Cobot coupling system : (a) coupling mechanism detail , and (b) two robots coupled together.

and propulsion actuation, as well the management of the extension modules.

The docking ports provide multiple functions: they (1) enable the connection between the robot and a charging dock, they (2) provide a physical, solid connection between robots (stacking) for cooperative tasks such as faster transportation of heavy loads. For charging, the stacking of multiple robots also enables daisy-chained charging across several robots, thus saving space. A detailed view of the docking ports is provided on Figure 3.

Two possible applications of the robot are telepresence and object manipulation. Telepresence can be performed using the onboard display, speakers, and microphone. Our design has enough space for a common tablet-sized display. Mobile manipulation is crucial for robot-environment interaction. A robotic arm with a gripper is provided on the bottom part of the robot, providing several manipulation capabilities such as cargo transportation. This module fits in a standard module bay and can be replaced for additional guest module space.

For safer operation, electric propulsion was used instead of pressurized gas. Along with this, we also feature electromagnetic and acoustic noise reduction methods by using grounded copper mesh on the vehicles construction and acoustic absorptive materials around the motors airflow tunnel. With this, we aim at long periods of operation aboard space stations.

III. PROPULSION MODEL

Consider a single propeller i whose motor is rigidly linked to the body frame \mathcal{B} , as depicted in Figure 4. This propeller generates a reaction force (thrust) \bar{F}_i and torque \bar{M}_i on the vehicle body. While the former results directly from the propeller thrust,

$$\bar{F}_i = f_i \hat{u}_i \quad f_i = K_1 u_i \quad (1)$$

where u_i is the actuation signal and f_i is the scalar thrust, the later is the sum of two components: the torque caused by the non-central thrust and the propeller reaction torque:

$$\bar{M}_i = \bar{r}_i \times \bar{F}_i - \tau_i \hat{u}_i \quad \tau_i = w_i K_2 u_i \quad (2)$$

where \times denotes vector cross product and w_i is -1 or 1 depending on whether the propeller rotates clockwise or anti-clockwise for a positive forward thrust $f_i > 0$. These linear relationships result from the momentum-blade element

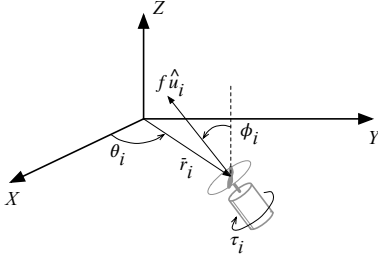


Fig. 4: Notation used for modeling a single propeller with respect to the body frame \mathcal{B} , centered on the vehicle's CoM.

theory by considering $u = n^2$, where n is the blade's rotation speed (in revolutions per second) while the constants K_1 and K_2 given by

$$K_1 = \rho D^4 C_T \quad K_2 = \frac{\rho D^5}{2\pi} C_P \quad (3)$$

where ρ is the air density, D is the propeller diameter, and the C_T and C_P are blade dependent adimensional constants called thrust and power coefficients [10].

The relative position \bar{r}_i of the i -th propeller, orthogonal to the Z axis, and the unit vector \hat{u}_i , aligned with the propeller axis, are uniquely defined by the angles θ_i and ϕ_i , and can be easily obtained from geometrical reasoning by:

$$\bar{r}_i = \begin{pmatrix} d \cos(\theta_i) \\ d \sin(\theta_i) \\ 0 \end{pmatrix} \quad \hat{u}_i = \begin{pmatrix} \sin(\theta_i) \sin(\phi_i) \\ -\cos(\theta_i) \sin(\phi_i) \\ \cos(\phi_i) \end{pmatrix} \quad (4)$$

where $d = \|\bar{r}_i\|$ is the distance from the propeller to the CoM. Stacking together the resulting force \bar{F}_i and torque \bar{M}_i , one can obtain the linear relation

$$\begin{pmatrix} \bar{F}_i \\ \bar{M}_i \end{pmatrix} = \bar{a}_i u_i \quad (5)$$

where

$$\bar{a}_i = \begin{pmatrix} K_1 \hat{u}_i \\ K_1 \bar{r}_i \times \hat{u}_i - w_i K_2 \hat{u}_i \end{pmatrix} = \begin{pmatrix} K_1 \sin(\theta_i) \sin(\phi_i) \\ -K_1 \cos(\theta_i) \sin(\phi_i) \\ K_1 \cos(\phi_i) \\ [K_1 d \cos(\phi_i) - w_i K_2 \sin(\phi_i)] \sin(\theta_i) \\ -[K_1 d \cos(\phi_i) - w_i K_2 \sin(\phi_i)] \cos(\theta_i) \\ -K_1 d \sin(\phi_i) - w_i K_2 \cos(\phi_i) \end{pmatrix} \quad (6)$$

For a vehicle with N propellers, the resulting force and torque will be given by the sum of the contributions of each propeller, given with respect to the CoM, by (5). This sum can be put in matrix form as

$$\begin{pmatrix} \bar{F} \\ \bar{M} \end{pmatrix} = \mathbf{A} \bar{u} \quad (7)$$

where $\mathbf{A} = [\bar{a}_1 \cdots \bar{a}_N]$ is a square matrix, hereby called *actuation matrix*, and $\bar{u} = [u_1 \cdots u_N]^T$ is the actuation input vector. *The crucial observation is that, if the actuation matrix \mathbf{A} has at least rank 6, the linear equation (7) can be solved for \bar{u} for any given combination of \bar{F} and \bar{M} .* A necessary

(but not sufficient¹) condition for this to be true is to have at least 6 propellers, thus justifying the hexarotor design considered in this paper. Note that this matrix only depends on the vehicle's design parameters, defined by the angles $\{\theta_i\}$ and $\{\phi_i\}$, distance d , the trust coefficients K_1 , K_2 , and $\{w_i\}$.

IV. OPTIMIZATION OF THE DESIGN PARAMETERS

In this section we will study how the design parameters translate to the actuation matrix \mathbf{A} defined in the previous section. In particular, we will consider how actuation limits translates into maximum values of force and torque. We will then optimize these parameters in order to maximize the upper bound of forces and torques, over all directions, imposed by a bounded actuation.

A. Problem statement

We will start by considering that each actuation signal is bounded between -1 and 1 , that is,

$$-1 \leq u_i \leq 1 \quad \text{for } i = 1, \dots, 6 \quad (8)$$

According to (7), this hypercube will map onto a 6-dimensional convex polyhedron² in the (\bar{F}, \bar{M}) space. Any other choice of bounds is possible by appropriately scaling constants K_1 and K_2 . However, it assumes that the maximum propeller trust is symmetric with respect to the direction of rotation³. The remaining parameters are the angles $\{\phi_i\}$. We will base our analysis on the optimization of these angles with respect to various criteria.

Our goal will be to find the configurations of angles $\{\phi_i\}$ that maximize the range of forces (and torques) over all directions. Geometrically, this corresponds to changing $\{\phi_i\}$ such that a ball of nonzero radius can fit inside the 3-dimensional convex polyhedron in the \bar{F} space mapped by the actuation hypercube in (8), while keeping zero torque, $\bar{M} = 0$. A similar reasoning applies to the torque space \bar{M} , while keeping $\bar{F} = 0$.

First, we will address the problem of computing the maximum force along a given direction specified as a unit vector \hat{e} , while maintaining a zero torque. From (7), and assuming that \mathbf{A} is full rank, we get

$$\bar{u} = \mathbf{A}^{-1} \begin{pmatrix} \bar{F} \\ \bar{M} \end{pmatrix} = \mathbf{A}^{-1} \begin{pmatrix} F \hat{e} \\ 0 \end{pmatrix} \quad (9)$$

where $F > 0$ is the force magnitude. For what follows, it will be convenient to express the \mathbf{A}^{-1} matrix as blocks of three dimensional row vectors:

$$\mathbf{A}^{-1} = \begin{bmatrix} b_1^T & c_1^T \\ \vdots & \vdots \\ b_6^T & c_6^T \end{bmatrix} \quad (10)$$

¹Sufficiency required \mathbf{A} to be full rank.

²A convex polyhedron is an intersection of a finite number of half-spaces [11].

³Propellers may have different thrust capabilities along each direction of the rotation axis. The approach presented here can be easily extended to account for that asymmetry.

where $b_i, c_i \in \mathbb{R}^3$. Then, the actuation of the i -th propeller is given by

$$u_i = F b_i^T \hat{e} \quad (11)$$

Since $|u_i| \leq 1$, we have $F |b_i^T \hat{e}| \leq 1$, and thus F has this upper bound:

$$F \leq \frac{1}{|b_i^T \hat{e}|} \quad (12)$$

Since this inequality has to be satisfied for all propellers $i = 1, \dots, 6$, the maximum force $F_{\hat{e}}^{\max}$ is given by the lowest of these upper bounds

$$F_{\hat{e}}^{\max} = \min_i \frac{1}{|b_i^T \hat{e}|} \quad (13)$$

This force is the maximum force along a given direction \hat{e} . The maximum force attainable in any direction can be obtained by minimising this force over all possible directions. Since $|b_i^T \hat{e}| \leq \|b_i\|$, this minimum is given by

$$F^{\max} = \min_i \frac{1}{\|b_i\|} \quad (14)$$

The same reasoning can be applied to the torques: consider a torque $\bar{M} = M \hat{e}$ along an arbitrary direction defined by \hat{e} , the corresponding actuation with $\bar{F} = 0$ is $u_i = M c_i^T \hat{e}$, resulting in the following maximum torque along any direction:

$$M^{\max} = \min_i \frac{1}{\|c_i\|} \quad (15)$$

Now, these maximum forces and torque values depend on the design parameters. In the following we will use an optimization approach to find the values of these parameters that maximize the maximum force and/or torque. We will consider the propellers to be equally distributed radially, that is,

$$\theta_i = (i - 1) \frac{\pi}{3} \quad (16)$$

and a fixed distance d , as well as the constants K_1 and K_2 . All the remaining parameters will be the unknown variables:

$$\bar{\psi} = (\phi_1, \dots, \phi_6, w_1, \dots, w_6)^T \quad (17)$$

with the feasibility domain defined by

$$\Psi = \{\bar{\psi} : |\phi_{1,\dots,6}| \leq \phi_{\max}, w_{1,\dots,6} \in \{-1, 1\}\} \quad (18)$$

where ϕ_{\max} is the maximum allowed deviation from the vertical. As a mechanical constraint to allow obstructionless air flow we considered $\phi_{\max} = \pi/3$ in this work.

We can restate the maximization of (14) and (15) using the epigraph form [12], thus getting rid of the maximization of a minimum, in exchange of the introduction of two new variables, p and q :

$$\begin{aligned} & \text{minimize } p \\ & \text{subject to:} \\ & p \geq \|b_i\|^2, i = 1, \dots, 6 \end{aligned} \quad (19)$$

for the force and

$$\begin{aligned} & \text{minimize } q \\ & \text{subject to:} \\ & q \geq \|c_i\|^2, i = 1, \dots, 6 \end{aligned} \quad (20)$$

for the torque, where $\{b_i\}$ and $\{c_i\}$ depend non-linearly on the parameters $\bar{\psi}$ through the inverse of the actuation matrix \mathbf{A} as (10). In this form, the optimization variables are augmented with the cost, that is, $\bar{\psi}_p = (p, \bar{\psi})$ for the problem (19) and $\bar{\psi}_q = (q, \bar{\psi})$ for (20). It can be readily seen that these forms maximize (14) and (15), where the resulting maximum forces and torques can be recovered using $F^{\max} = 1/\sqrt{p}$ and $M^{\max} = 1/\sqrt{q}$.

B. Multi-criteria optimization

The design optimization aims at maximizing simultaneously two objective functions, force and torque ranges, given bounded actuation (8). To do so we will take a multi-criteria optimization approach [13], combining the optimization problems (19) and (20) into a single multi-criteria problem:

$$\begin{aligned} & \text{minimize } (p, q) \\ & \text{subject to:} \\ & p \geq \|b_i\|^2, i = 1, \dots, 6 \\ & q \geq \|c_i\|^2, i = 1, \dots, 6 \end{aligned} \quad (21)$$

In this problem, the optimization variables are augmented with both p and q , $\bar{\psi}_{pq} = (p, q, \bar{\psi})$, and we have two cost functions, say $J_1(\bar{\psi}_{pq}) = p$ and $J_2(\bar{\psi}_{pq}) = q$. The solution of this multi-criteria optimization problem is the set \mathcal{P} of non-dominated solutions, defined by: $\bar{\psi}_{pq}^0 \in P$ if and only if there is no $\bar{\psi}_{pq} \in \Psi$ such that $J_i(\bar{\psi}) \leq J_i(\bar{\psi}^0)$ for all $i \in \{1, 2\}$ and $J_i(\bar{\psi}) < J_i(\bar{\psi}^0)$ for at least one $i \in \{1, 2\}$. This set is also called *Pareto optimal set* [13], a subset of the *objective space* defined by all $(J_1(\bar{\psi}), J_2(\bar{\psi}))$ for $\bar{\psi} \in \Psi$.

Apart from very simple cases, the Pareto optimal set is not trivial to obtain exactly. Thus, we will make a pointwise approximation using the Normally Boundary Intersection (NBI) method [14]. This method is guaranteed to obtain Pareto optimal points if the objective space is convex. But it is still capable of obtaining points in “sufficiently concave” parts of the objective space [14].

The first step of NBI is to obtain the minimizers of the each cost function taken individually. These are also called *shadow minima*. Let us start by considering the first minimization problem (19), where $\bar{\psi}_p^*$ is the minimizer with minimum cost p^* . Then, this minimizer both minimizes p in (21) and, together with $q^0 = \max_i \|c_i\|^2$, is a non-dominated solution of (21), and thus belongs to its Pareto optimal set. This results from the fact that this q^0 is the smallest one that still satisfies the constraints of (21): any (p^*, q) with $q > q^0$ is dominated by (p^*, q^0) . The same reasoning can be applied to (20), resulting in the minimizer $\bar{\psi}_q^*$, with minimum cost q^* , that together with $p^0 = \max_i \|b_i\|^2$ is also a non-dominated solution of (21), thus also belonging to its Pareto optimal set.

On the (p, q) space, these two non-dominated solutions corresponds to two extremal points, (p^*, q^0) and (p^0, q^*) , of the Pareto optimal set: no feasible solutions exists neither to the left of p^* nor lower than q^* . *The application of NBI to a two cost function problem amounts to scanning along*

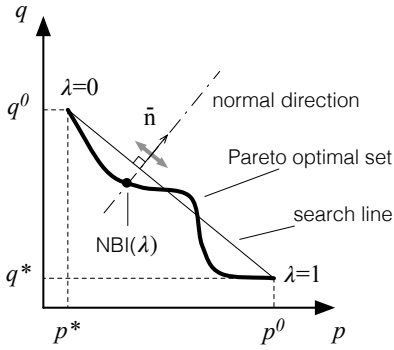


Fig. 5: Illustration of the NBI method: given a point defined by $\lambda \in [0; 1]$, along the search line between (p^*, q^0) and (p^0, q^*) , the optimization is done along the normal direction spawned by vector \bar{n} , resulting on the $NBI(\lambda)$ intersection point.

a straight line joining (p^*, q^0) and (p^0, q^*) , and then, for each point on this straight line, to determine the single non-dominated solution along the orthogonal direction.

Figure 5 illustrates the NBI method. This straight line can be parametrized by a λ value ranging between 0 and 1, resulting in $(1 - \lambda)(p^*, q^0) + \lambda(p^0, q^*)$. An orthogonal direction to this straight line is spawned by the vector $\bar{n} = (q^0 - q^*, p^0 - p^*)$. Using again the epigraph form, but now along this vector, we obtain the following constrained optimization problem:

$$\begin{aligned} & \text{minimize } t \\ & \text{subject to:} \\ & (q^0 - q^*)t + (1 - \lambda)p^* + \lambda p^0 \geq \|b_i\|^2 \\ & (p^0 - p^*)t + \lambda q^* + (1 - \lambda)q^0 \geq \|c_i\|^2 \\ & \text{for } i = 1, \dots, 6 \end{aligned} \quad (22)$$

with the augmented vector $\bar{\psi}_t = (t, \bar{\psi})$ as optimization variable. For a given $\lambda \in [0; 1]$, the solution of this optimization problem yields a minimizer $\bar{\psi}_t^*(\lambda)$ from which the corresponding point in the (p, q) space is

$$NBI(\lambda) = (p_\lambda, q_\lambda), \quad p_\lambda = \min_i \|b_i\|^2, \quad q_\lambda = \min_i \|c_i\|^2 \quad (23)$$

from which the maximum values of force and torque can be recovered as above mentioned.

Since these problems cannot be solved in closed form, we will make use of numerical optimization methods. The following section presents the numerical results obtained for this problem.

C. Numerical results

The optimization problem in (22) shows some features that make it non-trivial to solve: it is both strongly non-convex with mixed continuous and discrete variables. First, we will factor out the discrete part by iteratively trying each combination of $\{w_i\}$ values modulo rotations (also called

*orbits*⁴): from its $2^6 = 64$ possible combinations, only 14 correspond to combinations where no pair can be made equal after rotating one of them. Second, we use a random multistart initialization together with a convex optimization algorithm: for each sample drawn uniformly from the $\{\phi_i : |\phi_i| \leq \phi_{max}\}$ cube, we run the Constrained Optimization BY Linear Approximation (COBYLA) algorithm [15], as implemented in the SciPy optimization package.

To make the relation between force and actuation dimensionless, we divided the actuation matrix by K_1 . This way, the only dependence on physical coefficients of this matrix is on the parameters d and the ratio K_2/K_1 . Using (3), this ratio can be expressed as

$$\frac{K_2}{K_1} = \frac{D}{2\pi} \frac{C_P}{C_T} \quad (24)$$

For various small propellers (of about 4") we found⁵ this ratio to be approximately 0.01. And thus we used this value to obtain the numerical results presented in this section. For d we used the one from the design presented in Section II, that is, $d = 0.16$.

The extremes of the NBI search line are the shadow minima, *i.e.*, the minima of (19) and (20). For 1000 random initializations, we obtained these values for the shadow minima: $(p^*, q^0) = (0.250, 15.01)$ and $(p^0, q^*) = (0.4167, 9.728)$.

With these values, we ran our optimization method for λ ranging from 0 to 1 on 0.01 steps, for 1000 random initializations each. The result is a set of points approximating the Pareto optimal set, shown in Figure 6. The (a) plot of this figure suggests a convex Pareto front. For a range of λ values from 0 to about 0.4, the (p, q) values are constant. As λ increases over 0.4, there is a drop on the values of q , meaning a slight increase on M^{max} .

Table I shows some of the optimal configurations obtained for some values of λ . In our choice we decided to prefer maximum force, since the corresponding maximum torque is not significantly lower than other non-dominated solutions, and thus we selected a configuration found in the lower range of λ values. We rounded off the angle values to the closest integer degree, resulting in the configuration shown in Table II. All of the following results shown in this paper employ this selected configuration.

V. POSITION AND ATTITUDE CONTROL

This section addresses the problem of designing a convergent position and attitude controller for the vehicle.

The dynamical model of the vehicle, in the absence of gravity, can be derived from the Newton and Euler equations of motion. Let us denote the position and velocity of the body frame \mathcal{B} with respect to the inertial frame \mathcal{I} as \bar{x} and \bar{v} , the rotation matrix of frame \mathcal{B} with respect to \mathcal{I} as \mathbf{R} , and the angular velocity of the vehicle in the body frame \mathcal{B} as $\bar{\omega}$.

⁴For instance, $[1, -1, 1, 1, 1, 1]$ and $[1, 1, -1, 1, 1, 1]$ belong to the same orbit, and thus it is redundant to try both of them.

⁵We used the UIUC Propeller Data Site, Vol. 2, <http://m-selig.ae.illinois.edu/props/propDB.html> (retrieved Nov-2015).

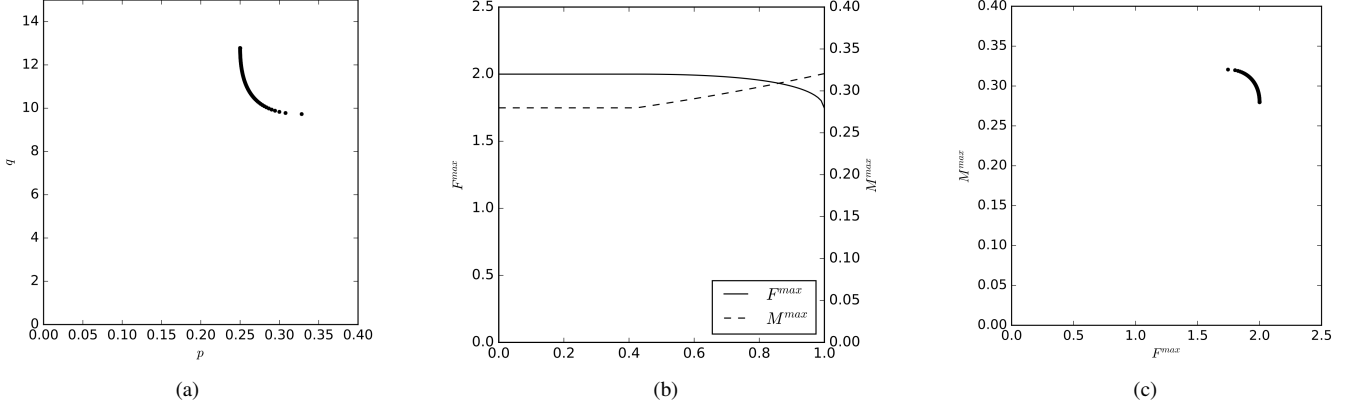


Fig. 6: Pointwise approximation to the Pareto optimal set using the NBI method: (a) obtained points in the (p, q) space, (b) F^{max} and M^{max} in function of λ , and (c) in the (F^{max}, M^{max}) space. The dimensions for F^{max} and M^{max} have no physical meaning because of the division of the actuation matrix by K_1 , as explained in the text, and thus are to be understood in relative terms only.

λ	ϕ_1	ϕ_2	ϕ_3	ϕ_4	ϕ_5	ϕ_6	w_1	w_2	w_3	w_4	w_5	w_6	F^{max}	M^{max}
0	54.74	-54.73	54.74	-54.74	54.73	-54.74	-1	1	-1	1	-1	1	2.000	0.2798
0.25	54.73	-54.74	54.74	-54.73	54.74	-54.74	-1	1	-1	1	-1	1	2.000	0.2798
0.5	53.73	-53.73	53.73	-53.73	53.73	-53.73	-1	1	-1	1	-1	1	1.999	0.2844
0.75	49.56	-49.56	49.56	-49.56	49.56	-49.56	-1	1	-1	1	-1	1	1.969	0.3009
1	38.84	-38.85	38.84	-38.84	38.85	-38.84	-1	1	-1	1	-1	1	1.745	0.3206

TABLE I: Some of the configurations obtained for 5 equally spaced values of λ . The values for $\{\phi_i\}$ are shown in degrees. As before, the dimensions for F^{max} and M^{max} have no physical meaning.

propeller (i)	1	2	3	4	5	6
θ_i	0	60	120	180	240	300
ϕ_i	55	-55	55	-55	55	-55
w_i	-1	1	-1	1	-1	1

TABLE II: Design parameters of the selected solution. Both $\{\theta_i\}$ and $\{\phi_i\}$ are expressed in degrees.

Then,

$$\begin{cases} \dot{\bar{x}} = \bar{v} \\ m\dot{\bar{v}} = \mathbf{R}\bar{F} \\ \dot{\mathbf{R}} = \mathbf{R}\mathbf{S}(\bar{\omega}) \\ \mathbf{J}\dot{\bar{\omega}} = \bar{M} - \bar{\omega} \times \mathbf{J}\bar{\omega} \end{cases} \quad (25)$$

where the constants m and \mathbf{J} are the vehicle's mass and moment of inertia, while $\mathbf{S}(\bar{\omega})$ is the skew-symmetric matrix defined by

$$\mathbf{S}(\bar{\omega}) = \begin{bmatrix} 0 & -\omega_z & \omega_y \\ \omega_z & 0 & -\omega_x \\ -\omega_y & \omega_x & 0 \end{bmatrix} \quad (26)$$

for $\bar{\omega} = [\omega_x \ \omega_y \ \omega_z]^T$.

The approach used for the motion control of the vehicle exploits its holonomic design by decoupling the translational and rotational modes. To do so, we first apply feedback linearisation [16] to the translational part of (25):

$$\begin{cases} \dot{\bar{x}} = \bar{v} \\ \dot{\bar{v}} = \bar{p} \\ \bar{F} = m\mathbf{R}^T\bar{p} \end{cases} \quad (27)$$

and then design a feedback controller for \bar{p} . Since this dynamical system is diagonal and second order, a PD controller is enough to ensure exponential convergence:

$$\begin{aligned} \bar{e}_x &= \bar{x} - \bar{x}_d \\ \bar{e}_v &= \bar{v} - \bar{v}_d \\ \bar{p} &= -k_x\bar{e}_x - k_v\bar{e}_v \end{aligned} \quad (28)$$

where \bar{x}_d and \bar{v}_d are the desired position and velocity vectors in the inertial frame \mathcal{I} , and k_x and k_v are the proportional and derivative gains of the PD controller.

For the attitude control we follow the exponentially convergent $SO(3)$ controller proposed in [17]:

$$\begin{aligned} \bar{e}_R &= \frac{1}{2\sqrt{1 + \text{tr}[\mathbf{R}_d^T\mathbf{R}]}} S^{-1}(\mathbf{R}_d^T\mathbf{R} - \mathbf{R}^T\mathbf{R}_d) \\ \bar{e}_\omega &= \bar{\omega} - \mathbf{R}^T\mathbf{R}_d\bar{\omega}_d \\ \bar{M} &= -k_R\bar{e}_R - k_\omega\bar{e}_\omega \\ &\quad + \mathbf{S}(\mathbf{R}^T\mathbf{R}_d\bar{\omega}_d)\mathbf{J}\mathbf{R}^T\mathbf{R}_d\bar{\omega}_d + \mathbf{J}\mathbf{R}^T\mathbf{R}_d\dot{\bar{\omega}}_d \end{aligned} \quad (29)$$

where \mathbf{R}_d is the rotation matrix of the desired attitude, $\bar{\omega}_d$ is the desired angular velocity vector, with k_R and k_ω as controller gains. The S^{-1} function performs the inverse operation as the one defined in (26), that is, recovers the vector from a given skew-symmetric matrix.

VI. SIMULATION RESULTS

In order to validate of the proposed design, we simulated a model of our robot with V-REP simulation framework [18].

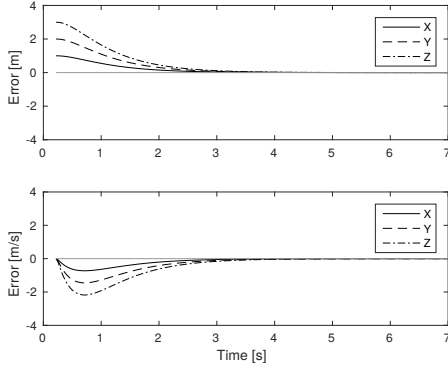


Fig. 7: Translational mode error convergence, from top to bottom: e_x and e_v .

Here, we kept the size of the vehicle and estimated the real mass and inertia of the fully loaded robot. The design parameters used are the ones shown in Table II. The vehicle mass is 6.05kg. In V-REP we simulated the force and torque produced by each propeller as modeled in (1) and (2). Thus, this simulation includes the validation of both the design discussed in Section IV and the controller proposed in Section V.

The validation was divided in two phases: on the first, each motion mode (translation and attitude) is evaluated separately, and on the second, we simulated a path defined by a sequence of waypoints with attitude setpoints and a unmodeled payload transportation, thus combining both modes simultaneously. In the last case we added noise to the pose with a variance of 2cm on position, 2cm/s on velocity, 5° on attitude and $1^\circ/\text{s}$ on angular velocity.

A. Individual motion mode

For this validation, the robot is holding on position (0, 0, 1), while the reference is set at (1, 2, 4). The total movement of the robot is 1, 2 and 3 meters along X, Y and Z axis. On Figure 7 we provide the obtained results for position convergence with the proposed controller in (27) and (28). Convergence rates are equal across all axis as expected. It only depends on the gains (equal for all axis) and the mass of the vehicle.

On the attitude simulation, we start the vehicle at $(0^\circ, 0^\circ, 0^\circ)$ and the reference is set as $(70^\circ, -50^\circ, 30^\circ)$ (both in XYZ Euler angles). The results are shown in Figure 8. Attitude convergence is approximately the same on all axis. As it depends only on the gains (equal for all axis) and the inertia of the vehicle (almost diagonal due to its symmetry), this result was also expectable.

B. Waypoint navigation and payload transportation

To validate the joint position and attitude control, we used waypoint navigation: we created a virtual path composed by 6 waypoints, varying on both position and attitude. The trajectory followed by the vehicle is represented on 9. Plotted are both the X and Y axes of the body frame \mathcal{B} to represent its attitude. We retrieved the errors across the whole trajectory

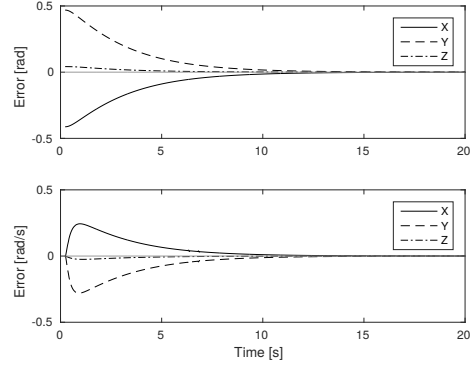


Fig. 8: Attitude mode error convergence, from top to bottom: e_R and e_ω .

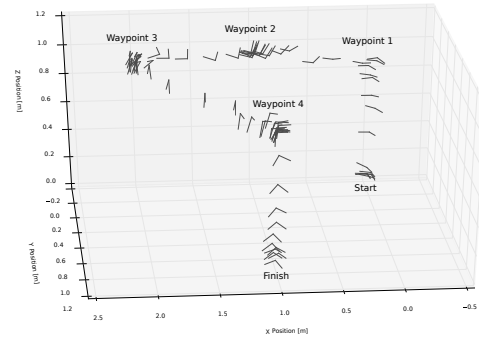


Fig. 9: Trajectory followed by the robot without load. Plotted are X and Y axis of the inertia frame \mathcal{I} .

following, for both position and attitude. These are shown in Figure 10.

Then, we added a non-modeled payload to the system: a sphere with 6Kg of mass — about the same mass of the vehicle. Even with such payload, the controller was able to converge to the required positions, though taking significantly more time. Shown on Figure 11 are screenshots of the vehicle along its 3 waypoint trajectory: 1 meter up along Z and 1 meter right along Y. The position and attitude errors for this trajectory are plotted on Figure 12

VII. CONCLUSIONS AND FUTURE WORK

This paper presented a design of a modular holonomic hexarotor robot for microgravity environments. The propulsion is based on 6 propellers oriented in such a way that both holonomy is attained and the minimum upper bound of the thrust across all directions is maximized.

We used a multi-criteria optimization approach to guide the design parameters of the proposed propulsion system. We also include a convergent controller for the vehicle, and a validation of our design in a realistic physics-based simulator. Simulation results show the vehicle navigating between waypoints. In particular, we show that the convergence to the waypoints is robust to localization noise and to unmodeled dynamics, such as attachment to heavy loads.

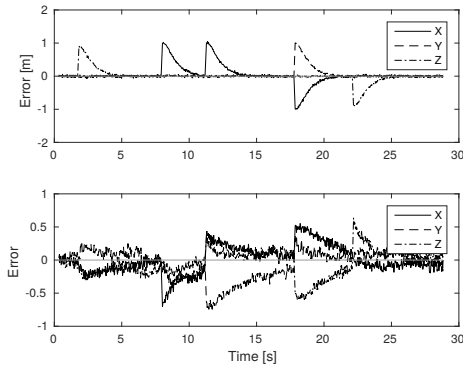


Fig. 10: Position (on top) and attitude (on bottom) errors along the no-load trajectory of Figure 9.

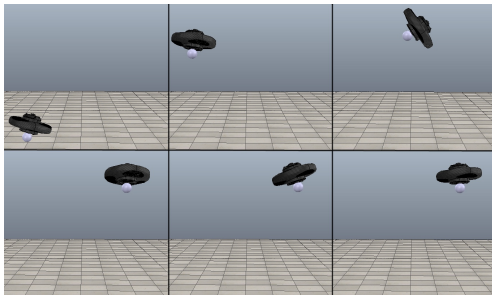


Fig. 11: Trajectory followed by the robot with 6kg non-modeled load. Pictured are six positions of the robot along its trajectory.

A real implementation of Space CoBot will face several challenges. One of them is the asymmetry of propeller trust depending on the rotation direction can be addressed by appropriately scaling the u to rotation speed mapping. Other issues include modeling the motor and propeller inertia and the quadratic relation between propeller speed and thrust⁶.

Future work will address: (1) vision-based navigation using the onboard camera array, (2) mobile dexterous manipulation with the onboard robotic arm, encompassing both single robot and cooperative multirobot, and (3) robustify the controller to better handle unmodeled dynamics, such as heavy loads. We will also aim at constructing a prototype for validating the design both in 2D motion, e.g., frictionless table on Earth, and in microgravity testbeds, e.g., in a parabolic flight aircraft.

REFERENCES

- [1] D. Miller, A. Saenz-Otero, J. Wertz, A. Chen, G. Berkowski, C. Brodel, S. Carlson, D. Carpenter, S. Chen, S. Cheng, D. Feller, S. Jackson, B. Pitts, F. Perez, J. Szuminski, and S. Sell, "SPHERES: a testbed for long duration satellite formation flying in micro-gravity conditions," in *Proceedings of the AAS/AIAA Space Flight Mechanics Meeting*, 2000.
- [2] S. Nolet, A. Saenz-Otero, D. W. Miller, and A. Fejzic, "SPHERES operations aboard the iss: Maturation of gn&c algorithms in micro-gravity," in *30th Annual AAS Guidance and Control Conference*, 2007, pp. 7–42.

⁶The lower the propeller speed is, a higher change in its speed is needed to achieve the same change in force.

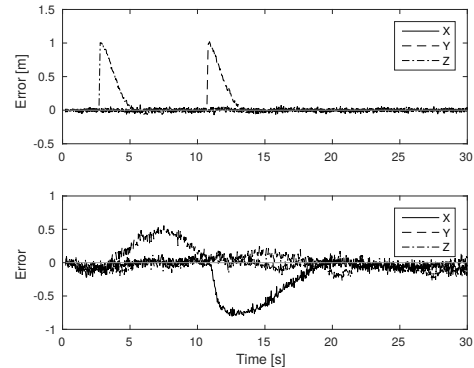


Fig. 12: Position (on top) and attitude (on bottom) errors with non-modeled 6kg load along the trajectory of Figure 11.

- [3] M. Bualat, J. Barlow, T. Fong, C. Provencher, T. Smith, and A. Zuniga, "Astrobee: Developing a free-flying robot for the international space station," in *AIAA SPACE 2015 Conference and Exposition*, 2015.
- [4] G. Jiang and R. Voyles, "Hexrotor UAV platform enabling dextrous interaction with structures – flight test," in *IEEE International Symposium on Safety, Security, and Rescue Robotics (SSRR)*, 2013, pp. 1–6.
- [5] R. Voyles and G. Jiang, "Hexrotor UAV platform enabling dextrous interaction with structures – preliminary work," in *IEEE International Symposium on Safety, Security, and Rescue Robotics (SSRR)*, 2012, pp. 1–7.
- [6] S. Rajappa, M. Ryll, H. H. Bühlhoff, and A. Franchi, "Modeling, control and design optimization for a fully-actuated hexarotor aerial vehicle with tilted propellers," in *2015 IEEE International Conference on Robotics and Automation (ICRA)*. IEEE, 2015, pp. 4006–4013.
- [7] K. Kiso, T. Ibuki, M. Yasuda, and M. Sampei, "Structural optimization of hexrotors based on dynamic manipulability and the maximum translational acceleration," in *2015 IEEE Conference on Control Applications (CCA)*. IEEE, 2015, pp. 774–779.
- [8] D. Langkamp, G. Roberts, A. Scillitoe, I. Lunnon, A. Llopis-Pascual, J. Zamecnik, S. Proctor, M. Rodriguez-Frias, M. Turner, A. Lanzon, and W. Crowther, "An engineering development of a novel hexrotor vehicle for 3d applications," in *International Micro Air Vehicle conference and competitions 2011 (IMAV-2011)*, 2011.
- [9] P. Roque and R. Ventura, "Space cobot: a collaborative aerial robot for indoor microgravity environments," arXiv:1602.03573v1 [cs.RO], 2016.
- [10] B. W. McCormick, *Aerodynamics, aeronautics, and flight mechanics*, 2nd ed. John Wiley & Sons, 1995.
- [11] M. Jeter, *Mathematical programming: an introduction to optimization*. CRC Press, 1986, vol. 102.
- [12] S. Boyd and L. Vandenberghe, *Convex optimization*. Cambridge university press, 2004.
- [13] R. Statnikov and J. B. Matusov, *Multicriteria Optimization and Engineering*. Chapman & Hall, 1995.
- [14] I. Das and J. E. Dennis, "Normal-boundary intersection: A new method for generating the pareto surface in nonlinear multicriteria optimization problems," *SIAM Journal on Optimization*, vol. 8, no. 3, pp. 631–657, 1998.
- [15] M. J. D. Powell, *Advances in Optimization and Numerical Analysis*. Springer, 1994, ch. A Direct Search Optimization Method That Models the Objective and Constraint Functions by Linear Interpolation, pp. 51–67.
- [16] S. Sastry, *Nonlinear Systems: Analysis, Stability, and Control*. Springer, 1999.
- [17] T. Lee, "Exponential stability of an attitude tracking control system on SO(3) for large-angle rotational maneuvers," *Systems & Control Letters, Elsevier*, vol. 61, no. 1, pp. 231–237, 2012.
- [18] E. Rohmer, S. P. N. Singh, and M. Freese, "V-REP: a versatile and scalable robot simulation framework," in *International Conference on Intelligent Robots and Systems (IROS)*, 2013.